Mesoporous Hydrous Manganese Dioxide Nanowall Arrays with Large Lithium Ion Energy Storage Capacities

By *Dawei Liu, Betzaida Battalla Garcia, Qifeng Zhang, Qing Guo, Yunhuai Zhang, Saghar Sepehri,* and *Guozhong Cao**

Novel nanowall arrays of hydrous manganese dioxide $MnO_2 \cdot 0.5H_2O$ are deposited onto cathodic substrates by the potentiostatic method from a mixed aqueous solution of manganese acetate and sodium sulfate. The deposition is induced by a change of local pH resulting from electrolysis of H_2O, and hierarchical mesoporous nanowall arrays are formed as a result of simultaneous precipitation of manganese hydroxide and release of hydrogen gas bubbles from the cathode. The morphology and lithium ion intercalation properties are found to change appreciably with the concentration of the precursor electrolyte, with a significant reduction in specific surface area with an increased precursor concentration. For example, mesoporous nanowall arrays deposited from 0.1 M solution possess a surface area of $\sim$96 $m^2\ g^{-1}$ and exhibit a stable high intercalation capacity of 256 mA hg^{-1} with a film of 0.5 μm in thickness, far exceeding the theoretical limit of 150 mA hg^{-1} for manganese dioxide bulk film. Such mesoporous nanowall arrays offer much greater energy storage capacity (e.g., $\sim$230 mA hg^{-1} for films of $\sim$2.5 μm) than that of anodic deposited films of the same thickness ($\sim$80 mA hg^{-1}). Such high lithium ion intercalation capacity and excellent cyclic stability of the mesoporous nanowall arrays, especially for thicker films, are ascribed to the hierarchically structured macro- and mesoporosity of the $MnO_2 \cdot 0.5H_2O$ nanowall arrays, which offer large surface to volume ratio favoring interface Faradaic reactions, short solid-state diffusion paths, and freedom to permit volume change during lithium ion intercalation and de-intercalation.

1. Introduction

As the demand for rechargeable lithium ion batteries is experiencing a huge rise in recent years, the suitable electrode materials has focused on finding alternative cathodic materials to replace the commercialized lithium cobalt oxide electrode, which has the disadvantage of high cost and toxicity.[1,2] Manganese dioxide, which has been used in primary lithium batteries and alkaline batteries for decades, is a well accepted electrode material for clean energy storage because of its low cost, low toxicity, and chemical stability.[3,4] However, the application of manganese dioxide in secondary lithium ion batteries has been hindered by some practical problems, such as its relatively low intercalation capacity and poor cycle stability; bulk manganese dioxide film could only deliver a capacity of less than 120 mA hg^{-1} and the host structure was easily distorted by the lithium-ion insertion/extraction reactions, thus suffering poor stability over long-term cycles.[5,6] Nanostructuring is considered to be an effective way to enhance the intercalation capacity and improve the cyclic stability. By providing a large electrode–electrolyte contact area and a shorter diffusion path for both lithium ion and electron transportation,[7–10] nanostructuring has been reported to enhance the lithium ion storage capacity of MnO_2 to exciting values of more than 200 mA hg^{-1},[11–13] comparable to other high-capacity transitional metal oxides, such as nanostructured vanadium oxides.[14–16] The cyclic stability of manganese dioxide can also be improved by the application of mesoporous nanostructures. Mesopores embedded in the nanostructure act as a buffering layer to alleviate the adverse effect of volume expansion experienced during the intercalation/de-intercalation reactions, which was believed to be the main reason for the poor cyclic stability of bulk manganese dioxide.[17] Mesoporous SnO_2,[18] V_2O_5[19], and TiO_2[20–22] have all been successfully applied in the fabrication of lithium ion battery electrodes. The commonly adopted route to obtain mesoporous nanostructures of pure manganese dioxide is through hard-template-based fabrication of nanorods or nanoparticles using mesoporous silica as a template.[23,24] Such grown nanostructured manganese dioxide was highly mesoporous and proved to be capable of continuously delivering high lithium ion intercalation capacities.[25,26] However, this template-based fabrication was time-consuming and not cost-effective because of the utilization of a silica template. In addition, complete removal of the silica template after fabrication remains a technical challenge.

---

[*] Prof. G. Z. Cao, D. W. Liu, B. B. Garcia, Dr. Q. F. Zhang,
Dr. S. Sepehri
Department of Materials Science and Engineering
University of Washington, Seattle 98195 (USA)
E-mail: gzcao@u.washington.edu

Q. Guo
Department of Mechanical Engineering
University of Washington, Seattle 98195 (USA)

Dr. Y. H. Zhang
Department of Chemical Engineering
Chongqing University
Chongqing 400030 (China)

DOI: 10.1002/adfm.200801515

Template-free fabrication of mesoporous MnO_2 has therefore become an important destination. Recently, successful fabrication of high-surface-area manganese dioxide following the template-free concept has been reported by Sinha et al. by means of a wet precipitation method[27] and its application in extensive air purification has turned out to be a great success. However, manganese dioxide fabricated in this way is not suitable as large lithium-ion capacity storage device as the electrolyte penetration would be very difficult in such thick oxide films with small pores. Porous graphite[28] and titania nanotube arrays[29] offer better porous structures for lithium ion battery electrodes, as they consist of both macropores and mesopores. Macropores facilitate easy access of electrolyte to the electrode films, while mesopores offer the desired large surface area for Faradaic reactions and short distances for both mass and charge diffusion in solid.[30] Various attempts to fabricate a variety of macroporous metal oxides have been reported, for example, NiO nanoflowers.[31] The combination of macroporous and mesoporous structures was also reported in V_2O_5[32] to improve lithium ion intercalation kinetics. However, most porous manganese oxide possesses a relatively low specific surface area of $\sim 13\,m^2\,g^{-1}$,[33,34] and thus demonstrates limited progress in lithium ion intercalation capacity and kinetics as well as cyclic stability. In this paper, we reported the fabrication of hierarchically structured mesoporous manganese dioxide nanowall arrays on cathodic substrates by means of water-electrolysis-induced precipitation, similar to our earlier work on nanostructured vanadium pentoxide.[35] Such grown hierarchically structured manganese dioxide electrodes delivered a high lithium ion intercalation capacity with much improved cyclic stability. Deposition parameters affecting the porous structure, nanostructure, and the lithium-ion intercalation properties were studied and discussed.

2. Results and Discussion

2.1. Growth of Hierarchically Structured Films on Cathodic Substrate

Figure 1 shows typical scanning electron microscopy (SEM) and transmission electron microscopy (TEM) images of manganese oxide film grown on cathodic substrate under an externally applied voltage of −1.8 V. Figure 1a is the SEM topomorphology image, and clearly indicates that the deposited film on cathodic substrate consisted of hierarchical nanowall arrays with large voids of micrometers in diameter. The cross-section SEM image (Fig. 1b) reveals that the nanowall structure was deposited with no continuous film at the interface between the Pt film and manganese oxide nanowall arrays. Study by TEM suggests that the nanowalls might not have a dense structure (Fig. 1c).

Figure 2 shows the typical nitrogen sorption isotherm of the cathodic-deposited manganese oxide nanowall arrays and the pore size distribution calculated from the nitrogen sorption isotherm. The isotherm of cathodic-deposited manganese oxide nanowall arrays was of typical IV-type curve with a clear H1-type hysteretic loop, characteristic of mesoporous materials.[17] The Brunauer–Emmett–Teller surface area of the sample was $96.2\,m^2\,g^{-1}$. This large surface area is comparable to the surface

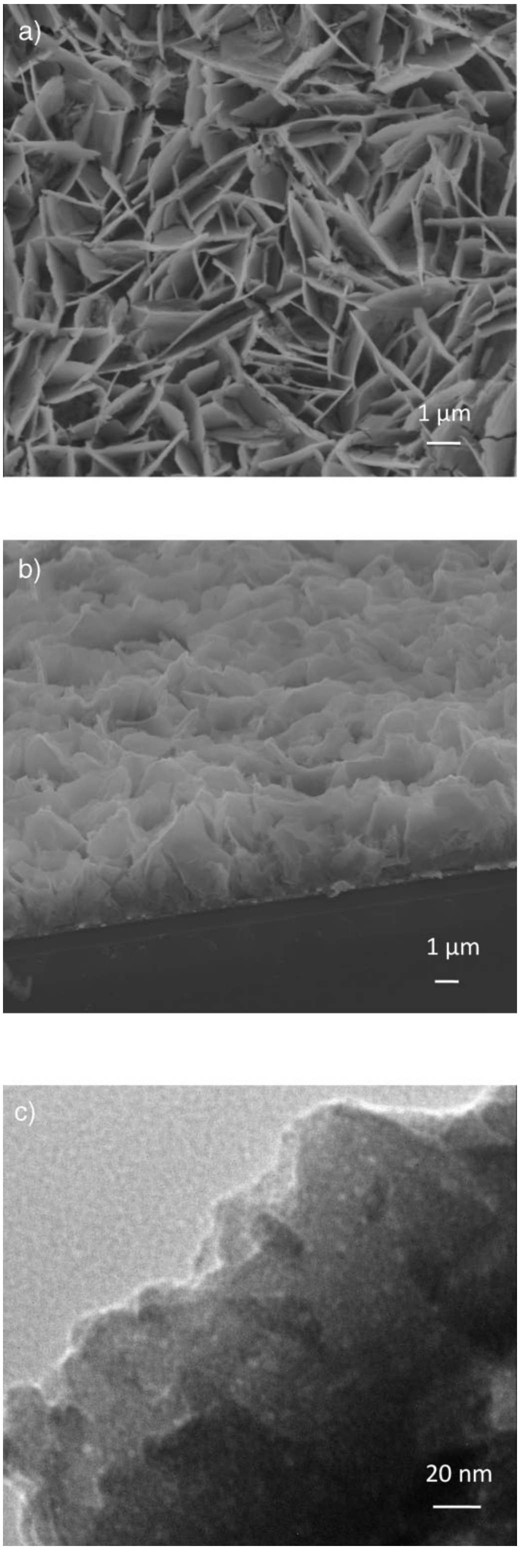

Figure 1. a) SEM top-view image of hierarchically structured nanowall arrays deposited on cathodic substrate by means of water-electrolysis-induced precipitation from 0.1 M precursor solution (manganese acetate and sodium sulfate) at a voltage of −1.8 V for 15 min. b) SEM side-view image of the same nanowall arrays. c) TEM image of nanowall structure from the same deposition.

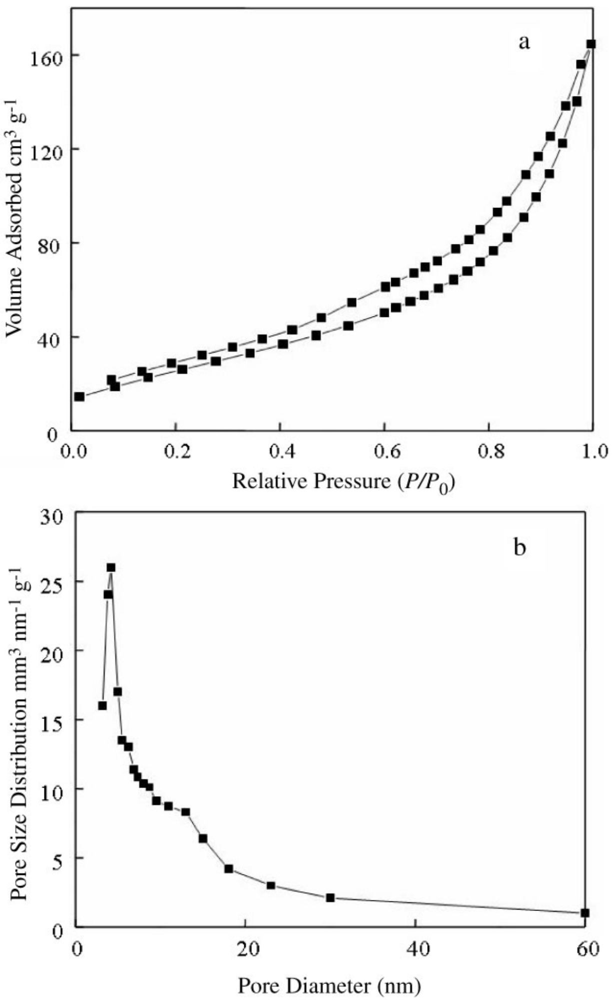

Figure 2. a) Nitrogen sorption isotherm measured at 77 K of the powder samples, the manganese oxide nanowall arrays scratched from cathodic substrates deposited from the 0.1 M electrolyte and under an externally applied voltage of −1.8 V and b) the pore size distribution in the manganese oxide nanowall array samples calculated from the nitrogen sorption isotherm.

area of template fabricated mesoporous manganese dioxide, around 91 $m^2\ g^{-1}$.[36] It is also higher than recently reported manganese dioxide nanowires (~69 $m^2\ g^{-1}$)[37] and self-assembled mesoporous-nanostructured manganese oxide (~70 $m^2\ g^{-1}$).[38] The macropores discernible on the SEM images could not account solely for such a large surface area; in fact, 76.1 $m^2\ g^{-1}$ of the 96.2 $m^2\ g^{-1}$ came from mesopores with the pore size distribution centered at a diameter of 4.2 nm.

The formation of such a large number of mesopores in the deposited structure can be understood by considering the growth mechanism of the cathodic deposition used in our experiment, that is, water-electrolysis-induced precipitation, which included the electrolysis of water at the cathode surface, an increase in local pH at the vicinity of the cathode, reaction with OH^-, and then precipitation of manganese hydroxide on the cathode.[13,39] The deposition was the result of the above-mentioned sequential process that occurred at the surface or in the vicinity of the cathode. At first, when an appropriate voltage was applied, the water electrolysis occurred at the cathode surface, generating hydrogen gas, and OH^- groups:

$$2H_2O + 2e^- = H_2 + 2OH^- \tag{1}$$

The generated OH^- groups then bond with Mn^{2+} ions, causing nanoparticle precipitation:

$$Mn^{2+} + 2OH^- = Mn(OH)_2 \tag{2}$$

The precipitation growth mechanism scheme is depicted by Figure 3a: during the precipitation, the metal substrate surface consists of two kinds of sites; one where the nanoparticles of manganese hydroxide precipitate and another where hydrogen gas bubbling occurs (no precipitation). This discontinuous precipitation on the substrate generates the macroporous nanowall arrays. In addition, in every precipitation cluster, the spaces between neighboring nanoparticles were mesopores, as shown by TEM and the nitrogen isotherm study. Exactly the same nanostructure as that depicted by the growth mechanism scheme was observed when the precursor concentration was tuned to a very large amount. In Figure 3b and c, SEM and TEM images clearly indicate that the deposited hierarchical nanowall arrays were formed by closely stacked spherical nanoparticles with diameters of ~50 nm. During the deposition, water electrolysis provided not only the OH^- groups that bonded with Mn^{2+} to precipitate manganese hydroxide nanoparticles but also generated H_2 gas bubbles, which acted as the force to prevent continuous precipitation on the whole substrate, thus producing the macropores of the nanowall arrays. Similar macroporous and mesoporous hierarchical structures was also found in cathodic deposited $Co(OH)_2$.[40]

Solution precipitation is a well-developed technique for fabricating transitional metal hydroxide or oxide. The fundamental concept is the bonding of metal ions and base group OH^- to generate metal hydroxide nanoprecipitates, such as the deposition of $Ni(OH)_2$.[41] The classical precipitation method works through the addition of base, changing the whole pH of the electrolyte. However, the water-electrolysis-induced precipitation method we used here created only a local high-pH region near the working electrode, without affecting the whole electrolyte pH environment; thus, the nanostructure could be directly deposited onto the working electrode. Moreover, hydrogen bubbles with sizes of tens of nanometers were generated in the process[42] and, in our experiments, they assisted in the formation of the macropores in the nanowall arrays.

After the deposition, when the film was exposed to air, air oxidation turns the unstable manganese hydroxide into hydrous manganese dioxide[43]

$$2Mn(OH)_2 + O_2 = 2MnO_2 + 2H_2O \tag{3}$$

In these experiments, the oxidation process was said to be complete when the film turned completely black (the characteristic color of manganese dioxide[44]) from white-yellow (the characteristic color of manganese hydroxide[44]). After X-ray diffraction (XRD) and X-ray photoelectron spectroscopy studies,

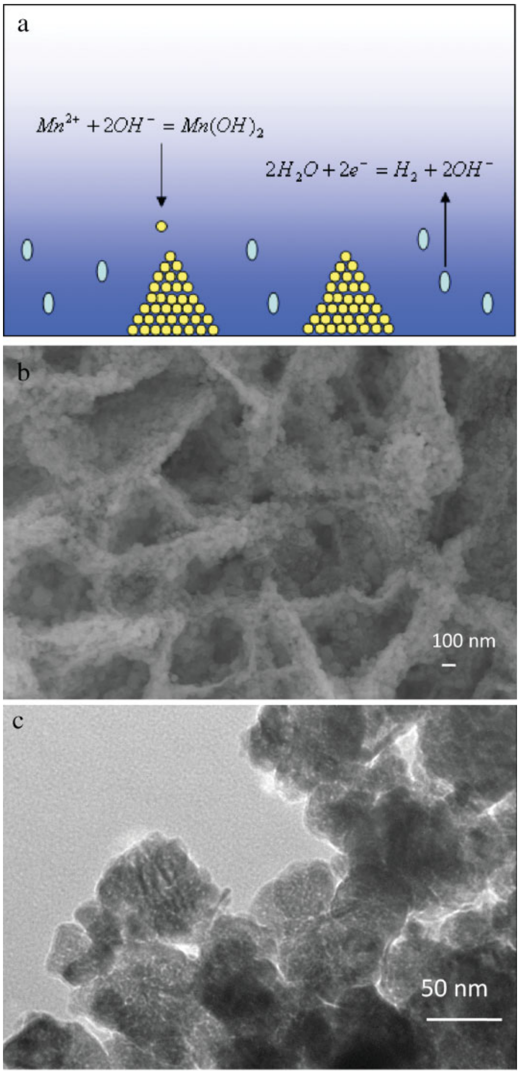

Figure 3. a) Scheme showing the proposed growth mechanisms of hierarchically structured manganese hydroxide nanowall arrays on cathodes due to the increased pH value resulting from water electrolysis (blue area stands for high pH); precipitation of manganese hydroxide nanoparticles from the electrolyte accompanied with the release of hydrogen gas bubbles from the cathode surface. b) SEM image of the hierarchically structured nanowall arrays mimicking the structure proposed in the growth mechanism scheme and c) TEM image of stacked nanoparticles in a nanowall with voids (pores).

and thermogravimetric analysis (TGA), the resultant film was characterized to be hydrous manganese dioxide $MnO_2 \cdot 0.5H_2O$, as reported in our earlier work.[13]

The effect of deposition voltage on product morphology was also studied and we found that when the cathodic voltage was -1.4 V or higher the substrate was not fully covered by deposition, nor was the film stable in the electrolyte for lithium ion intercalation measurements. When the deposition voltage was between -1.4 and -2.2 V, for example, -1.8 V, no major differences in specimen morphology were observed. However, when the deposition voltage was lower than -2.2 V, the bubbling phenomena was so fierce that a homogeneous film was very difficult to obtain.

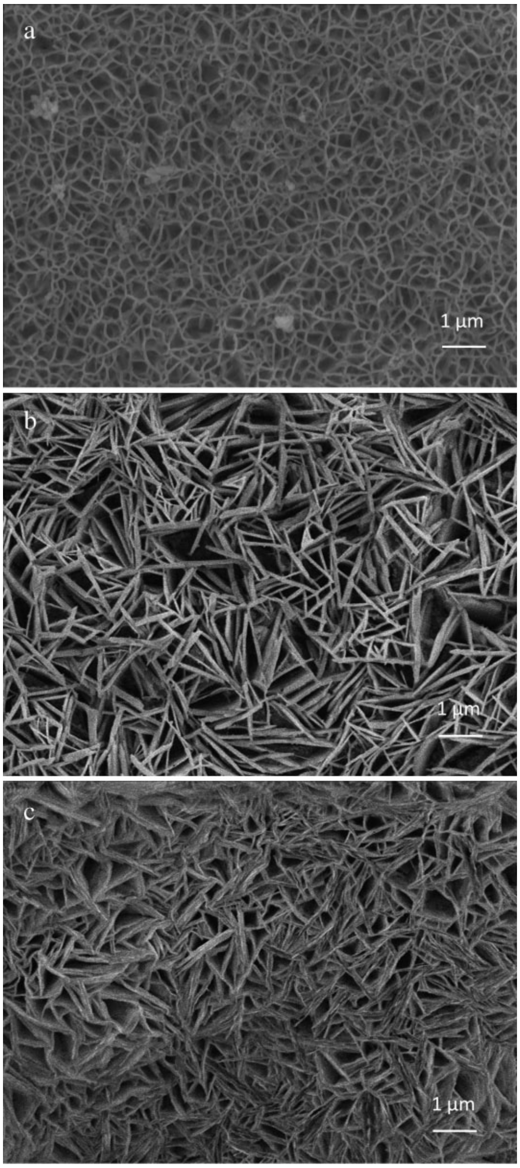

Figure 4. SEM top morphologies of the hierarchically structured nanowall arrays deposited on cathodic substrates using an externally applied voltage of -1.8 V for 15 min from precursor concentrations of a) 0.02 M, b) 0.1 M, and c) 0.5 M.

Figure 4 compares the SEM morphologies of cathodic deposited manganese dioxide from three different precursor concentrations; 0.02, 0.1, and 0.5 M. A comparison of these images shows that, when the precursor concentration was increased, the nanowall thickness was correspondingly enhanced, similar to what was reported of Zn–Al double hydroxide deposition.[45] The macropore size increased from around 500 nm for the 0.02 M specimen to around 1 μm for the 0.1 M specimen, but dropped back to around 500 nm for the 0.5 M specimen when the nanosheets became stuck together. Considering these varied morphologies for specimens deposited from varied precursor concentrations, different values of surface areas were also expected. Table 1 compares the surface areas of

Table 1. Brunauer–Emmett–Teller surface area and pore size distribution of cathodic deposited $MnO_2 \cdot 0.5H_2O$ nanowall arrays grown from different precursor concentrations.

Precursor concentration [M]	Total surface area [$m^2\ g^{-1}$]	Mesopore surface area [$m^2\ g^{-1}$]	Pore diameter [nm]
0.1	96.2	76.1	4.2
0.5	41.9	33.7	3.7
1	32.2	25.8	3.4

the 0.1, 0.5, and 1 M specimens; it was found that the surface area of the specimens reduced from 96 (0.1 M specimen) to 42 $m^2\ g^{-1}$ (0.5 M specimen) and finally to only 32 $m^2\ g^{-1}$ (1.0 M specimen). Since the mesopore sizes for the three specimens did not change so dramatically, this reduction is believed to be related to the nanowall thickness enlargement seen in the SEM images.

By variation of the deposition time it was possible to achieve different deposition thicknesses. The curve in Figure 5 displays the relationship between deposition time and product thickness; apart from the initial deposition thickness, below 0.5 μm, the thickness of the deposited film increased with deposition time nearly linearly. It took only 1 min for the thickness to reach 0.5 μm but around 6 min to reach 1.5 μm. After around 20 min, the thickness increased to 4.5 μm. The lower growth rate after the initial 0.5 μm deposition can be attributed to the reduced water electrolysis rate caused by the partially covered platinum substrate after initial deposition. The nearly linear relationship between the deposition time and deposition thickness is indicative that there was no change of the rate-limiting process and offers easy control of the film thickness. This linear relationship also suggests thicker films can be readily grown.

2.2. Lithium Ion Intercalation Properties

The electrochemical properties of the as-fabricated mesoporous nanowall arrays were measured by using lithium-ion-intercalation tests. Cyclic voltammograms (CV) of the 0.1 M specimen in the first and tenth cycles are compared in Figure 6a. In the first cycle, the anodic peak was centered on 0.15 V, corresponding to lithium ion extraction, and the cathodic peak was centered on −0.85 V, corresponding to lithium ion insertion. As could be clearly seen, after 10 cycles the cathodic peaks shifted a little, to higher voltages, but the swept area of the voltammograms did not change greatly, indicating good stability of the nanowall arrays in the cyclic measurements.

Figure 6b displays the first and tenth cycle chronopotentiometric (CP) discharge/charge curves of the deposited nanowall arrays with the deposition thickness around 0.5 μm. The first cycle discharge curve dropped initially in a sloping manner to around −0.6 V, and then a discharge plateau appeared with around 100 mA hg^{-1} delivered in this region before the curve reached the lower voltage limit of −1.4 V in a sloping manner again. Eventually, the whole discharge capacity reached a value as high as 256 mA hg^{-1}, equal to the lithium intercalation ratio of 0.83 Li per MnO_2, comparable to the recently reported MnO_2 nanocomposites[46] and much higher than the theoretical limit of 154 mA hg^{-1} for bulk MnO_2. The charge curve jumped quickly to

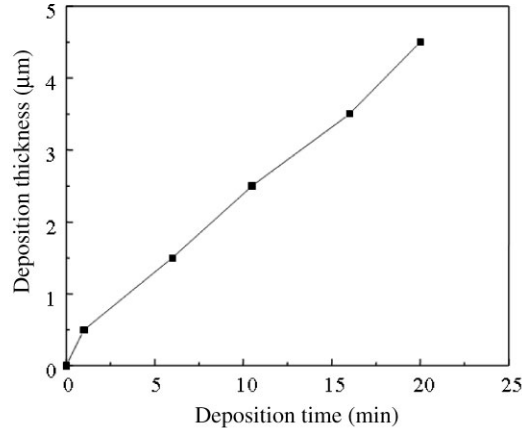

Figure 5. The dependence of the nanowall array thickness as a function of deposition time under a voltage of −1.8 V from 0.1 M precursor solution. The linear relationship suggests there is no change of the rate-limiting step during the entire deposition duration investigated in this study.

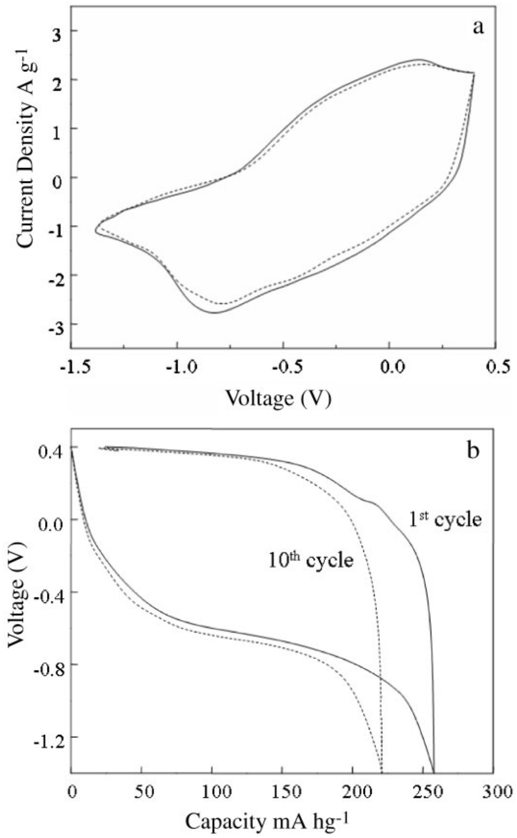

Figure 6. a) Cyclic voltammetry curves of the −1.8 V deposited $MnO_2 \cdot 0.5H_2O$ nanowall arrays in the first cycle (solid line) and tenth cycle (dashed line) in 1 M $LiClO_4$ propylene carbonate with a scan rate of 10 mV s^{-1} in a voltage range between 0.4 and −1.4 V versus Ag/AgCl and b) CP discharge/charge curves showing the lithium ion intercalation/deintercalation behaviors and capacities of 0.1 M and −1.8 V deposited $MnO_2 \cdot 0.5H_2O$ nanowall arrays with the deposition thickness 0.5 μm in the first and tenth cycle measured between 0.4 and −1.4 V versus Ag/AgCl at a current density of 30 mA g^{-1}.

around −0.1 V, then slowly returned to upper voltage limit of 0.4 V. The irreversible capacity was around 24 mA hg^{-1}, 10% of the discharge capacity. The tenth cycle curves possessed a similar shape as the first cycles; and, although, capacity decreased a little, the discharge capacity was still as high as 221 mA hg^{-1}. These high and over limit capacities could be attributed to two characteristics of the mesoporous $MnO_2 \cdot 0.5H_2O$ nanowall arrays. One was the low crystallinity of the cathodic-deposited MnO_2: the structure was less well packed, and thus possessed more open free space during lithium ion intercalation and diffusion as well as greater ability to accommodate structural deformation. The other explanation was the nanostructuring effect. Despite the fact that by now there is no detailed investigation of the intercalation mechanism for nanostructured MnO_2, frequently reported high discharge capacities over 200 mA hg^{-1}[47–49] have clearly indicated that nanostructured MnO_2, by providing a shorter diffusion path for lithium ions and reduced internal strain, could store a much higher ratio of lithium ions than the theoretical limit of bulk film. Similar phenomenon was also reported in nanostructured TiO_2.[50] Besides the high discharge capacities, the mesoporous nanowall arrays also demonstrated excellent electrochemical stability. After 10 cycles, the discharge capacity was still nearly 90% of the initial capacity. In addition to the reduced lattice strain offered by the nanostructure during cycling, the existence of mesopores in the nanowall arrays was also responsible for the cycle stability, because of their buffering role to the volume expansion experienced during redox reactions.

Figure 7 compares the initial CP discharge/charge curves of nanowall arrays deposited from different precursor concentrations, i.e., 0.1, 0.5, and 1 M of similar deposition thicknesses (around 2.5 μm). For all the discharge curves, the discharge plateau could be clearly observed between −0.7 and −0.8 V. A 0.1 M specimen had the highest capacity of 225 mA hg^{-1}, around 100 mA hg^{-1} of which was delivered by the sloping mannered intercalation before the discharge plateau appeared, and around 50 mA hg^{-1} was delivered after the plateau. As the concentration was increased to 0.5 M, the discharge capacity reduced to around 180 mA hg^{-1}, but the discharge capacity delivered on discharge plateau was still around 80 mA hg^{-1}, very similar to the 0.1 M specimen. The 1 M specimen had a further lower discharge capacity, reduced to 156 mA hg^{-1}, and this reduction was clearly seen to be the shrinkage of the plateau size in contrast to the 0.5 M specimen. All of these specimens exhibited very good reversibility: after a cycle of discharge/charge, the curves returned to near their starting points, leaving a gap of less than 20 mA hg^{-1}.

The initial CP discharge/charge curves of different deposition thicknesses ranging from 0.5 to 4.5 μm are compared in Figure 8a. As can be seen from the CP curves, there was a much less significant decrease of discharge capacity associated with an increase of deposition thickness. The discharge plateau shrinkage was also identified and can be seen graphically to be a factor in the capacity loss. The discharge capacities were 256, 243, 225, 223, and 201 mA hg^{-1} for 0.5, 1.5, 2.5, 3.5, and 4.5 μm, respectively. However, even when the deposition thickness was as large as 4.5 μm, the discharge capacity was still nearly 80% of that of small deposition thickness, that is, 0.5 μm. In addition, all the deposition thicknesses shared the characteristic of small irreversible capacities which created the nearly closed discharge/charge loops of the CP curves.

The long-term cycle performance of lithium ion intercalation/deintercalation capacities of different thicknesses was also measured by CP test, and compared in Figure 8b for the first

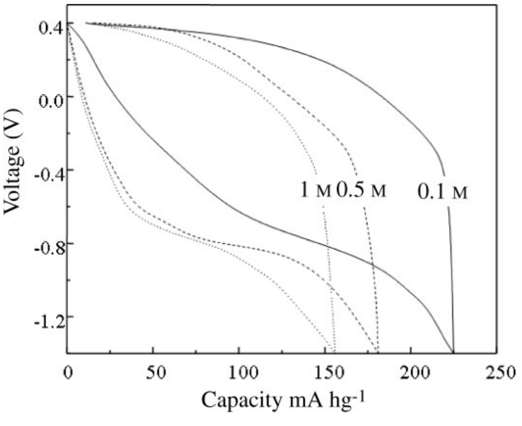

Figure 7. CP discharge/charge curves in the first cycle of $MnO_2 \cdot 0.5H_2O$ nanowall arrays deposited from precursor concentrations of 0.1, 0.5, and 1 M with the same deposition thickness (2.5 μm). The measurements were carried out between 0.4 and −1.4 V versus Ag/AgCl at a current density of 30 mA g^{-1}.

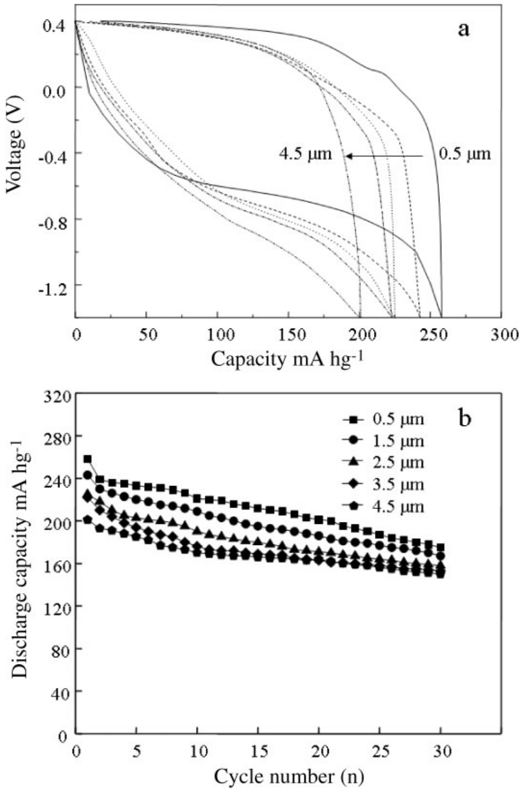

Figure 8. a) CP discharge/charge curves in the first cycle of $MnO_2 \cdot 0.5H_2O$ nanowall arrays of different deposition thicknesses from a precursor concentration of 0.1 M and b) their long-term cycle discharge capacities as a function of cycle number. The measurements were carried out between 0.4 and −1.4 V versus Ag/AgCl at a current density of 30 mA g^{-1}.

30 cycles. As can be clearly seen, for all the thicknesses the cathodic-deposited manganese dioxide exhibited stable high capacities over these cycles. In detail, the 0.5 μm sample began with a high discharge capacity of 256 mA hg^{-1}, which dropped to 239 mA hg^{-1} in the second cycle. The capacity then continued to drop slightly, although it remained as high as 175 mA hg^{-1} after 30 cycles. The 1.5-, 2.5-, 3.5-, and 4.5-μm samples exhibited similar performance; initially, they had values as high as 243, 225, 223, and 201 mA hg^{-1}, respectively. After 30 cycles, the discharge capacities were 167, 158, 153, and 150 mA hg^{-1} for each thickness. Compared with pure manganese dioxide nanowires fabricated by Park et al.,[37] which had an initial discharge capacity of 180 mA hg^{-1}, all the measured nanowall arrays delivered higher initial discharge capacities. After 30 cycles, the nanowall arrays exhibited capacities close to those of the nanowires after their second cycle; between 150 and 160 mA hg^{-1}. The larger surface area of the nanowall arrays (96 $m^2\ g^{-1}$) compared to the nanowires ($<69\ m^2\ g^{-1}$) should have contributed to the higher capacities in the initial cycles.

Another finding is that, for the mesoporous nanowall arrays, the discharge-capacity reduction was 22% when the deposition thickness was increased from 0.5 to 4.5 μm, and scaled at a rate of approximately 5% per μm.

2.3. Comparison with Anodic Deposited Manganese Dioxide

To make a comparison of lithium ion intercalation capacities, manganese dioxide was also prepared through an anodic oxidation route according to the literature.[51] In the lithium ion intercalation test, the anodic manganese dioxide was also measured for different deposition thicknesses, that is, 0.5, 1.5, and 2.5 μm, and the CP curves are shown in Figure 9a. In the thin film, the film could deliver a reasonably good value of 189 mA hg^{-1}. However, the discharge capacities reduced by more than 50% when the deposition film thickness increased from 0.5 to 2.5 μm and the curve shapes were different. When the film thickness was around 0.5 μm, there was an obvious discharge plateau in the voltage range between −0.7 and −0.8 V. Nearly half of the total discharge capacity of 189 mA hg^{-1} was delivered in this region. As the film were made thicker, the plateau disappeared. Thus, the initial discharge capacities were badly reduced to 112 and 79 mA hg^{-1} for 1.5 and 2.5 μm, 41 and 58% less, respectively. It was also noted that after the completion of one cycle of lithium ion intercalation and de-intercalation, none of these curves returned to the starting points. The 0.5-μm sample had a large capacity loss of around 43 mA hg^{-1}, 23% of the discharge capacity. The 1.5-μm sample had similar irreversible capacity of 41 mA hg^{-1}, 37% of the discharge capacity; while the 2.5-μm sample had a smaller irreversible capacity of 14 mA hg^{-1} but the irreversible ratio was still nearly 20%. The low coulombic efficiency (ratio of charge capacity to discharge capacity) of all these samples revealed the capability difference between lithium ion insertion and extraction for anodic deposited manganese dioxide. With the same reaction current density, a large portion of lithium ions inserted into the host could not be extracted. The cycle performance of different thicknesses in the first ten cycles is detailed in Figure 9b and compared with cathodic deposited manganese dioxide of the same thicknesses. It is obvious that cathodic deposited manganese dioxide possesses a higher discharge capacity and better stability over anodic deposited manganese dioxide for each thickness. The anodic deposited manganese dioxide only delivered reasonable initial discharge capacity (189 mA hg^{-1}) when the film thickness was around 0.5 μm. This value also dropped very quickly to 164 mA hg^{-1} in the second cycle and eventually to only 95 mA hg^{-1} in the tenth cycle, indicating a capacity degradation of 50%. For larger thicknesses, 1.5 and 2.5 μm, the discharge capacities were far below the values of their cathodic counterparts. A 1.5-μm sample began with a discharge capacity of 112 mA hg^{-1}, dropped to 95 mA hg^{-1} in the second cycle, and had only 66 mA hg^{-1} left in the tenth cycle (41% degradation). A 2.5-μm sample's discharge capacity began with an even smaller value of 79 mA hg^{-1}, dropped to 68 mA hg^{-1} in the second cycle, and was only 45 mA hg^{-1} in tenth cycle (43% degradation).

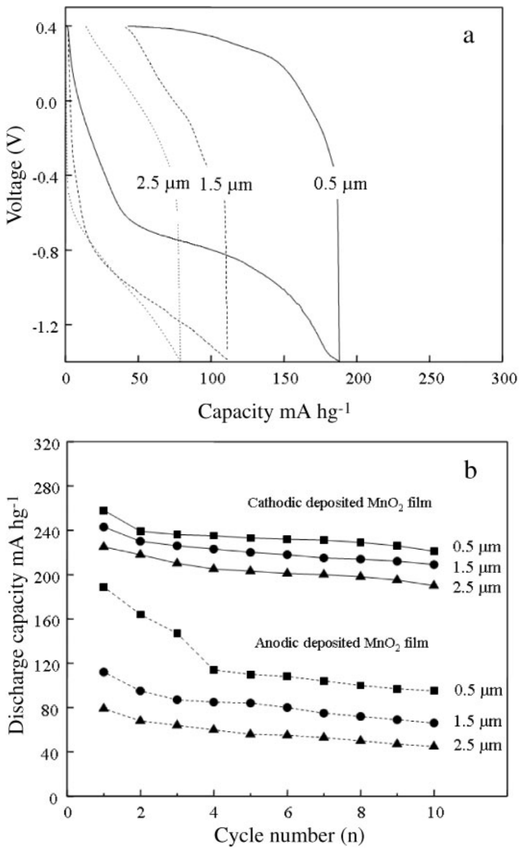

Figure 9. a) CP discharge/charge curves in the first cycle of anodic deposited manganese dioxide of different deposition thicknesses and b) the comparison of discharge capacities of anodic deposited manganese dioxide and cathodic deposited manganese dioxide in the first 10 cycles. The measurements were carried out between 0.4 and −1.4 V versus Ag/AgCl at a current density of 30 mA g^{-1}.

The above comparison clearly reveals that the cathodic deposited manganese dioxide films possessed favorable hierarchically mesoporous structure with higher discharge capacities and better cycle stability than anodic deposited manganese dioxide. The cycle stability can be attributed to the mesoporous structure of the cathodic deposited manganese dioxide nanowall arrays. As to the high discharge capacities at large deposition thickness, the macrostructure should be key; aside from the large surface area and shorter diffusion path provided for lithium ion reactions, this honeycomb macroporous structure facilitated the penetration of electrolyte to the bottom of the array in the same way as tube arrays, even when thickness was large, thus minimizing the adverse effect of large deposition thickness, that is, difficulty of electrolyte penetration. A similar phenomenon was also found when making a comparison of the thickness effect on vanadium oxide with and without macroporous structures.[52,53]

3. Conclusions

Hierarchically structured mesoporous nanowall arrays of $MnO_2 \cdot 0.5H_2O$ were grown on a cathodic substrate by means of water-electrolysis-induced precipitation. The mesoporous nanowall arrays were homogeneous throughout the whole thickness over the entire film with a large surface area of 96 m^2 g^{-1}. Deposition conditions such as externally applied voltage, precursor concentration, and deposition time were found to affect the mesoporous structure and lithium-ion intercalation properties of the grown films. The results showed that the nanowall arrays grown from 0.1 M electrolyte at −1.8 V possessed the best lithium ion intercalation capacity of 256 mA hg^{-1} for 0.5-μm-thick film. The nanowall arrays demonstrated excellent lithium ion intercalation properties not only for thin films but also for thick films; 4.5-μm film possessed a storage capacity >200 mA hg^{-1}. This excellent electrochemical performance of cathodic deposited mesoporous $MnO_2 \cdot 0.5H_2O$ nanowall arrays in lithium ion intercalation tests was due to its hierarchically macro- and mesoporous nanostructure: high surface area and short lithium ion diffusion path favored the interface Faradaic reactions and made a high reversible lithium ion intercalation capacity possible; the mesoporous structure provided more freedom for volume change and guaranteed cycle stability. In addition, the macroporous structure facilitated electrolyte penetration in thick-film deposition, permitting the growth necessary for thick-film fabrication.

4. Experiments

Materials and Synthesis: The precursor solutions were made by dissolving manganese acetate, $Mn(CH_3COO)_2 \cdot 4H_2O$ (99+%, Alfa Aesar) and anhydrous sodium sulfate, Na_2SO_4 (99%, J. T. Baker) into deionised (DI) water in a concentration of 0.1 M for both precursors. The solution was stirred at room temperature for 1 h to ensure the complete dissolution of both solutes prior to the electrodeposition experiments.

The cathodic deposition was carried out in a two-electrode deposition mode as reported in our previous work [13]. In brief, two electrodes were separated by a constant distance of 20 mm and the deposition was carried out at a constant voltage of −1.4, −1.8, and −2.2 V on cathodic Pt substrate. To investigate the effect of precursor concentration, different precursor concentrations from 0.02 to 1 M were also used for deposition under a voltage of −1.8 V and the deposition films were denoted by their precursor concentrations, e.g., film deposited from 0.5 M manganese acetate and anhydrous sodium sulfate solutions was denoted as the 0.5 M specimen. The effect of deposition time was also studied by changing the deposition time from 1 to 20 min on 0.1 M precursor under a voltage of −1.8 V. The products were then dried in a vacuum chamber and stored in a fume hood for 24 h until the originally white-yellow film turned black.

Characterization of Materials: As-obtained manganese oxide was characterized by means of XRD (Philips PW 1820), thermogravimetic analysis (TGA7, PerkinElmer), X-ray photoelectron spectroscopic (ESCA 210, VG Scientific Ltd.), scanning electron microscopy (JSM 7000, Philips JEOL), transmission electron microscopy (JSM 2010, Philips JEOL) and nitrogen adsorption–desorption at 77 K (NOVA 4200e, Quantachrome Instruments).

Electrochemical Characterization: The electrochemical properties of the manganese oxide on the Pt-coated substrates were investigated by using a conventional three-electrode system. Platinum foil was used as the counter electrode with an Ag/AgCl electrode employed as the reference electrode and 1 M $LiClO_4$ in propylene carbonate as the electrolyte solution for lithium ion intercalation experiments. Cyclic voltammogravic (CV) measurements were conducted in the voltage window of 0.4 and −1.4 V at a scan rate of 10 mV s^{-1}. CP measurements were carried out with the electric potential controlled between 0.4 and −1.4 V versus the standard Ag/AgCl reference electrode at a current density of 30 mA g^{-1}. Both the CVs and CPs were done by using an electrochemical analyzer (CH Instruments, Model 605B).

Acknowledgements

This work was supported in part by National Science Foundation (DMI-0455994 and DMR-0605159) and Air Force Office of Scientific Research (AFOSR-MURI, FA9550-06-1-0326). D. W. L. would like to acknowledge the graduate fellowship from the University of Washington Center for Nanotechnology (CNT). B. B. G. would like to acknowledge the fellowship from University of Washington Bioenergy IGERT (DGE-0654252). Y. H. Z. would like to acknowledge the fellowship from the Chinese Scholarship Council. Dr. Chongmin Wang at Pacific Northwest National Laboratory (PNNL) is acknowledged for the help with TEM pictures. Dr. Glen Fryxell and Dr. Nikki Lafemina at PNNL are acknowledged for the help with nitrogen isotherm measurement.

Received: October 10, 2008

---

[1] A. Manthiram, J. Kim, *Chem. Mater.* **1998**, *10*, 2895.
[2] J. S. Yang, J. J. Xu, *J. Power Sources* **2003**, *122*, 181.
[3] I. Taniguchi, C. K. Lim, D. Song, M. Wakihara, *Solid State Ionics* **2002**, *146*, 239.
[4] F. Leroux, D. Guyomard, *J. Phys. Chem. Solid* **2006**, *67*, 1303.
[5] C. S. Johnson, D. W. Dees, M. F. Mansuetto, M. M. Thackeray, D. R. Vissers, D. Argriyou, C. K. Loong, L. Christensen, *J. Power Sources* **1997**, *68*, 570.
[6] M. S. Whittingham, P. Y. Zavalij, *Solid State Ionics* **2000**, *131*, 109.
[7] J. W. Long, B. Dunn, D. R. Rolison, H. S. White, *Chem. Rev.* **2004**, *104*, 4463.
[8] S. Kobayashi, I. R. M. Kottegoda, Y. Uchimoto, M. Wakihara, *J. Mater. Chem.* **2004**, *14*, 1843.
[9] Y. Wang, K. Takahashi, H. M. Shang, G. Z. Cao, *J. Phys. Chem. B* **2005**, *109*, 3085.
[10] G. Z. Cao, D. W. Liu, *Adv. Colloid Interface Sci.* **2008**, *136*, 45.
[11] F. Y. Cheng, J. Z. Zhao, W. Song, C. S. Li, H. Ma, J. Chen, P. W. Shen, *Inorg. Chem.* **2006**, *45*, 2038.
[12] H. E. Wang, D. Qian, Z. G. Lu, Y. K. Li, R. J. Cheng, Y. J. Li, *J. Phys. Chem. Solids* **2007**, *68*, 1422.
[13] D. W. Liu, Q. F. Zhang, P. Xiao, B. B. Garcia, Q. Guo, R. Champion, G. Z. Cao, *Chem. Mater.* **2008**, *20*, 1376.
[14] Y. Wang, K. Takahashi, K. Lee, G. Z. Cao, *Adv. Funct. Mater.* **2006**, *16*, 1133.
[15] Y. Wang, G. Z. Cao, *Chem. Mater.* **2006**, *18*, 2787.
[16] Y. Wang, G. Z. Cao, *Adv. Mater.* **2008**, *20*, 2251.
[17] J. Y. Luo, J. J. Zhang, Y. Y. Xia, *Chem. Mater.* **2006**, *18*, 5618.
[18] Z. H. Wen, Q. Wang, Q. Zhang, J. H. Li, *Adv. Funct. Mater.* **2007**, *17*, 2772.
[19] P. Liu, S. H. Lee, C. E. Tracy, Y. Yan, J. A. Turner, *Adv. Mater.* **2002**, *14*, 27.

[20] D. Fattakhova-Rohlfing, M. Wark, T. Brezesinski, B. M. Smarsly, J. Rathousky, *Adv. Funct. Mater.* **2007**, *17*, 123.
[21] Y. G. Guo, Y. S. Hu, W. Sigle, J. Maier, *Adv. Mater.* **2007**, *19*, 2087.
[22] H. S. Zhou, D. L. Li, M. Hibino, I. Honma, *Angew. Chem. Int. Ed.* **2005**, *44*, 797.
[23] J. Y. Luo, Y. Y. Xia, *J. Electrochem. Soc.* **2007**, *154*, A987.
[24] H. R. Chen, X. P. Dong, J. L. Shi, J. J. Zhao, Z. L. Hua, J. H. Gao, M. L. Ruan, D. S. Yan, *J. Mater. Chem.* **2007**, *17*, 855.
[25] F. Jiao, P. Bruce, *Adv. Mater.* **2007**, *19*, 657.
[26] S. M. Zhu, H. S. Zhou, M. Hibino, I. Honma, M. Ichihara, *Adv. Funct. Mater.* **2005**, *15*, 381.
[27] A. K. Sinha, K. Suzuki, M. Takahara, H. Azuma, T. Nonaka, K. Fukumoto, *Angew. Chem. Int. Ed.* **2007**, *46*, 2891.
[28] K. T. Lee, J. C. Lytle, N. S. Ergang, S. M. Oh, A. Stein, *Adv. Funct. Mater.* **2005**, *15*, 547.
[29] D. W. Liu, P. Xiao, Q. F. Zhang, B. B. Garcia, Q. Guo, R. Champion, G. Z. Cao, *J. Phys. Chem. C* **2008**, *112*, 11175.
[30] N. Leventis, S. Mulik, X. J. Wang, A. Dass, C. Sotiriou-Leventis, H. B. Lu, *J. Am. Chem. Soc.* **2007**, *129*, 10660.
[31] X. M. Ni, Y. F. Zhang, D. Y. Tian, H. G. Zheng, X. W. Wang, *J. Crystal Growth* **2007**, *306, 418.*
[32] P. Liu, S. H. Lee, C. E. Tracy, J. A. Turner, J. R. Pitts, S. K. Deb, *Solid State Ionics* **2003**, *165*, 223.
[33] E. S. Toberer, R. Seshadri, *Adv. Mater.* **2005**, *17*, 2244.
[34] E. S. Toberer, T. D. Schladt, R. Seshadri, *J. Am. Chem. Soc.* **2006**, *128*, 1462.
[35] K. Takahashi, S. Limmer, Y. Wang, G. Z. Cao, *Jpn. J. Appl. Phys.* **2005**, *44*, 662.
[36] W. J. Zhou, J. Zhang, T. Xue, D. D. Zhao, H. L. Li, *J. Mater. Chem.* **2008**, *18*, 905.
[37] D. H. Park, S. H. Lee, T. W. Kim, S. T. Lim, S. J. Hwang, Y. S. Yoon, Y. H. Lee, J. H. Choy, *Adv. Funct. Mater.* **2007**, *17*, 2949.
[38] H. M. Chen, J. H. He, C. B. Zhang, H. He, *J. Phys. Chem. C* **2007**, *111*, 18033.
[39] G. H. A. Therese, P. V. Kamath, *Chem. Mater.* **2000**, *12*, 1195.
[40] S. M. Zhu, Z. Y. Zhou, D. Zhang, H. H. Wang, *Microporous Mesoporous Mater.* **2006**, *95*, 257.
[41] J. H. Chang, M. Park, D. Ham, S. B. Ogale, R. S. Mane, S. H. Han, *Electrochim. Acta* **2008**, *53*, 5016.
[42] A. Iwasaki, H. Kaneko, Y. Abe, M. Kamimoto, *Electrochim. Acta* **1998**, *43*, 509.
[43] A. Tomandl, M. Wolpers, K. Ogle, *Corros. Sci.* **2004**, *46*, 997.
[44] R. V. Lundquist in *Manganese Dioxide Prepared From Manganese Hydroxide*, US Department of the Interior, Bureau of Mines, Washington, DC, USA **1957**, Chapter 2.
[45] J. P. Liu, Y. Y. Li, X. T. Huang, G. Y. Li, Z. K. Li, *Adv. Funct. Mater.* **2008**, *18*, 1448.
[46] Y. G. Wang, W. Wu, L. Cheng, P. He, C. X. Wang, Y. Y. Xia, *Adv. Mater.* **2008**, *20*, 2166.
[47] B. B. Owens, S. Passerini, W. H. Smyrl, *Electrochim. Acta* **1999**, *45*, 215.
[48] J. J. Xu, G. Jain, J. Yang, *Electrochem. Solid-State Lett.* **2002**, *5*, A152.
[49] W. C. West, N. V. Myung, J. F. Whitacre, B. V. Ratnakumar, *J. Power Sources* **2004**, *126*, 203.
[50] M. Wagemaker, W. Borghols, F. Mulder, *J. Am. Chem. Soc.* **2007**, *129*, 4323.
[51] M. Q. Wu, L. P. Zhang, J. H. Gao, C. Xiao, D. M. Wang, A. Chen, S. R. Zhang, *J. Electroana. Chem.* **2008**, *613*, 125.
[52] C. Navone, J. P. Pereira-Ramos, R. Baddour-Hadjean, R. Salot, *J. Electrochem. Soc.* **2006**, *153*, A2287.
[53] K. L. Van, H. Groult, A. Mantoux, L. Perrigaud, F. Lantelme, R. Lindstroem, R. Badour-Hadjean, S. Zanna, D. Lincot, *J. Power Sources* **2006**, *160*, 592.